JNeurosci
THE JOURNAL OF NEUROSCIENCE

Research Articles: Development/Plasticity/Repair

Central nervous system hypomyelination disrupts axonal conduction and behaviour in larval zebrafish

https://doi.org/10.1523/JNEUROSCI.0842-21.2021

Cite as: J. Neurosci 2021; 10.1523/JNEUROSCI.0842-21.2021

Received: 19 April 2021
Revised: 11 August 2021
Accepted: 16 August 2021

Central nervous system hypomyelination disrupts axonal conduction and behaviour in larval zebrafish

Abbreviated title: CNS myelination in zebrafish circuit function

M.E. Madden[1], D. Suminaite[1], E. Ortiz[2], J.E. Early[1], S. Koudelka[1], M.R. Livesey[1,3], I.H. Bianco[4] , M. Granato[2], D.A. Lyons[1]

1. Centre for Discovery Brain Sciences, University of Edinburgh, Chancellor's Building, 49 Little France Crescent, Edinburgh BioQuarter, Edinburgh, EH16 4SB
2. Perelman School of Medicine, University of Pennsylvania, Philadelphia, PA 19104
3. Sheffield Institute for Translational Neuroscience, Department of Neuroscience, The University of Sheffield, Sheffield, S10 2HQ
4. Neuroscience, Physiology and Pharmacology, University College London, Gower Street, London, WC1E 6BT

Corresponding author email address: David A Lyons (David.Lyons@ed.ac.uk)

Figures: 5

Abstract: 238 words

Introduction: 619 words

Discussion: 1294 words

Acknowledgements: This work was supported by Wellcome Trust Senior Research Fellowships (102836/Z/13/Z and 214244/Z/18/Z) to DAL, a Wellcome Trust Edinburgh Clinical Academic Track PhD studentship (205042/Z/16/Z) to MEM, National Institutes of Health awards (MH109498 and NS118921) to MG, a National Institutes of Health NIDCD award (5T32DC016903) to EO, and a Sir Henry Dale Fellowship from the Royal Society & Wellcome Trust (101195/Z/13/Z) and a UCL Excellence Fellowship to IHB.

Abstract

Myelination is essential for central nervous system (CNS) formation, health and function. As a model organism, larval zebrafish have been extensively employed to investigate the molecular and cellular basis of CNS myelination, due to their genetic tractability and suitability for non-invasive live cell imaging. However, it has not been assessed to what extent CNS myelination affects neural circuit function in zebrafish larvae, prohibiting the integration of molecular and cellular analyses of myelination with concomitant network maturation. To test whether larval zebrafish might serve as a suitable platform with which to study the effects of CNS myelination and its dysregulation on circuit function, we generated zebrafish myelin regulatory factor (*myrf)* mutants with CNS-specific hypomyelination and investigated how this affected their axonal conduction properties and behaviour. We found that *myrf* mutant larvae exhibited increased latency to perform startle responses following defined acoustic stimuli. Furthermore, we found that hypomyelinated animals often selected an impaired response to acoustic stimuli, exhibiting a bias towards reorientation behaviour instead of the stimulus-appropriate startle response. To begin to study how myelination affected the underlying circuitry, we established electrophysiological protocols to assess various conduction properties along single axons. We found that the hypomyelinated *myrf* mutants exhibited reduced action potential conduction velocity and an impaired ability to sustain high frequency action potential firing. This study indicates that larval zebrafish can be used to bridge molecular and cellular investigation of CNS myelination with multiscale assessment of neural circuit function.

Significance statement

Myelination of central nervous system axons is essential for their health and function, and it now clear that myelination is a dynamic life-long process subject to modulation by neuronal activity. However, it remains unclear precisely how changes to myelination affects animal behaviour and underlying action potential conduction along axons in intact neural circuits. In recent years, zebrafish have been employed to study cellular and molecular mechanisms of myelination, due to their relatively simple, optically transparent, experimentally tractable vertebrate nervous system. Here we find that changes to myelination alter the behaviour of young zebrafish and action potential conduction along individual axons, providing a platform to integrate molecular, cellular and circuit level analyses of myelination using this model.

Introduction

Myelination is a well-characterised regulator of axonal health and function. In recent years it has become clear that myelination in the central nervous system (CNS) is dynamically regulated over time, including by neuronal activity, leading to the view that activity-regulated myelination might represent a form of functional plasticity (Fields, 2015). Furthermore, disruption to myelin is observed in numerous diseases of the CNS, and its regulation may represent a viable therapeutic strategy. Indeed, major insights have emerged from studies in multiple systems into the cellular and molecular mechanisms of CNS myelination, its regulation by neuronal activity, and its disruption in disease (Almeida, 2018; Gibson et al., 2018; Mount and Monje, 2017; Nave and Werner, 2014). In parallel, an increasing number of studies indicate that the generation of new oligodendrocytes (Geraghty et al., 2019; McKenzie et al., 2014; Pan et al., 2020; Steadman et al., 2020; Wang et al., 2020), and the degree of myelination (Bonnefil et al., 2019; Liu et al., 2016; Makinodan et al., 2012; Sampaio-Baptista et al., 2013), are important for distinct behaviours. However, how dynamic regulation of myelination, or disruption to myelin per se, actually affects the activity of circuits underlying these behaviours remains much less clear. This is partly due to the difficulty in visualising changes to myelination along single axons over time in the mammalian brain while concomitantly assessing their conduction properties and, in turn, evaluating how alteration to conduction affects neural circuit function.

Zebrafish are well established as a model organism for the study of myelination. The small size and transparency of their larvae, in combination with their genetic tractability and established transgenic tools, allows the assessment of myelin made by individual oligodendrocytes and along single axons in vivo e.g. (Auer et al., 2018; Koudelka et al., 2016). Together, these features have facilitated innumerable discoveries into the molecular and cellular mechanisms of myelination in this model (Preston and Macklin, 2015). Despite this progress, it remains unknown how CNS myelination affects the function of individual axons, neural circuits, or the behaviour of larval zebrafish, and thus it is not clear whether integrated multiscale assessments of CNS myelination from molecule through circuit can be performed in this model. However, it is now clear that larval zebrafish exhibit a diverse repertoire of experimentally tractable innate and stereotypical locomotor behaviours (Marques et al., 2018), many of which are mediated by reticulospinal (RS) neurons – a diverse set of neurons of the midbrain and hindbrain that process multimodal sensory information, and project descending axons to the spinal cord to coordinate specific motor outputs (Gahtan and O'Malley, 2003; Metcalfe et al., 1986). Intriguingly, RS axons are first to be myelinated in the zebrafish CNS and exhibit activity-regulated myelination

at larval stages (Almeida et al., 2011; Hines et al., 2015; Koudelka et al., 2016), implying that regulation of their myelination might influence circuit function in early larvae. In vivo electrophysiological recordings from subsets of individual RS neurons are feasible (Roy and Ali, 2013; Saint-Amant and Drapeau, 2003; Tanimoto et al., 2009), which in principle permits direct measurement of myelinated axon conduction properties underlying behaviour. However, how disruption to CNS myelination affects the behaviour or axonal conduction properties of larval zebrafish remains to be investigated.

In this study, we set out to investigate whether changes to CNS myelination can be detected in behaviour and in the conduction properties of single axons in zebrafish larvae. To achieve this, we created a myelin gene regulatory factor (*myrf*) mutant line, which exhibits severe CNS hypomyelination. Using this mutant, we demonstrate that both behavioural and electrophysiological consequences of hypomyelination are indeed detectable in the relevant circuitry in vivo, providing proof of principle that integrated analysis is feasible in this model organism, offering a framework for future investigations.

Materials and Methods

Zebrafish maintenance

Zebrafish were raised and maintained under standard conditions in the BVS Aquatics Facility in the Queen's Medical Research Institute, University of Edinburgh. Adult and larval animals were maintained on a 14 hours light and 10 hours dark cycle. Embryos were stored in 10mM HEPES-buffered E3 embryo medium or conditioned aquarium water with 0.000001% methylene blue at 28.5ºC. All experiments were performed under the project license 70/8436 with approval from the UK Home Office. The *myrf*^{ue70} line was maintained in a Tupfel Long Fin (TL) wildtype background. Within this manuscript, 'Tg' denotes a stable, germline inserted transgenic line.

Transgenic and mutant lines

The *myrf*^{ue70} mutant line was established during this study is described in this manuscript. The following transgenic lines were also used in this study: Tg(mbp:eGFP-CAAX) (Almeida et al., 2011; Mensch et al., 2015), Tg(mbp:nls-eGFP) (Karttunen et al., 2017).

Generation of myrf^{ue70} *mutants*

A freely available guide selection tool (http://crispr.mit.edu) was used to select sgRNA sequences against the second exon of the zebrafish myrf gene. sgRNA (target sequence CATTGACACCAGTATCCTGG) was synthesised using DNA template oligomers (5'-AAAGCACCGACTCGGTGCCACTTTTTCAAGTTGATAACGGACTAGCCTTATTTTAACTTGCTATTTCTAGCTCTAAAAC**CCAGGATACTGGTGTCAATG**CTATAGTGAGTCGTATTACGC-3') (Integrated DNA Technologies, Belgium) consisting of DNA coding for the T7 promotor, DNA recognition sequence (sgRNA variable region) and the sgRNA scaffold. sgRNA synthesis was performed using Ambion MEGAshortscript T7 Transcription Kit (Thermo Fisher Scientific) and the synthesised DNA oligomers as template. Transcribed sgRNA was purified using Ambion MEGAclear kit (Thermo Fisher Scientific). The expression vector for Cas9 protein, pCS2-nCas9n (Addgene plasmid #47929) (Jao et al., 2013), was used to transcribe Cas9 mRNA using the mMESSAGE mMachine SP6 kit (Thermo fisher Scientific) and purified using an RNeasy mini kit (Qiagen). Injection solutions were prepared with a final concentration of 300ng/µl nCas9n mRNA and 10ng/µl sgrNA in nuclease free water and 0.05% phenol red (Sigma Aldrich). Wildtype embryos

were injected at the single or two cell stage with 1.5nL injection solution. Injected F0 animals were raised to adulthood and outcrossed to wildtype animals to create F1 offspring. Clutches of F1 offspring were raised to adulthood and genotyped to identify heterozygous carriers of function disrupting mutant alleles. *myrf*^{ue70} refers to a specific allelic mutation consisting of the deletion of two cytosine nucleotides and insertion of a single adenine nucleotide (wildtype sequence: 5'-CCAGTAT**CC**TGGAGGAATA-3'; *myrf*^{ue70} mutant allele: 5'-CCAGTAT**A**TGGAGGAATA-3').

Genotyping

Tissue was genotyped using primers myrf-f (5' AACTGTGCGTAGGAACACGATA-3') and myrf-r (5'-TGGACCTCCGTGAAACAACTG-3') in a standard PCR reaction. The PCR product was digested using restriction enzyme PspGI (New England Biolabs), which cleaves wildtype product into 131bp and 157bp fragments. The mutant product remains uncut as the *myrf*^{ue70} allele contains a frameshifting indel which abolishes the PspGI cutting site. PCR products were visualised on a 2% gel following gel electrophoresis. All analyses were performed blinded to genotype.

Quantitative RT-PCR

Total RNA was extracted from whole brains of adult *myrf*^{ue70} wildtype and homozygous siblings using a modified Trizol RNA extraction protocol (TRIzol™ Reagent, Thermo Fisher Scientific). RNA concentration and integrity were assessed using a nanodrop spectrophotometer (NanoDrop One^{c}, Thermo Fisher Scientific). RNA clean-up was performed if necessary. cDNA synthesis was performed using Accuscript Hi Fidelity First Strand Synthesis kit (Agilent). The amount of RNA entered into the reaction was normalised between samples. Primers mbp-f (5'-ACAGAGACCCCACCACTCTT-3)' and mbp-r (5'-TCCCAGGCCCAATAGTTCTC-3') were used to amplify mbp transcripts within a qPCR reaction (Brilliant III Ultra-fast SYBR Green qPCR Master Mix, Agilent). Transcript levels were detected using Roche Light Cycler 96 (Roche Life Science) with the following amplification protocol: preincubation 95º for 180s, two step amplification 40 cycles: 95º for 10s then 60º for 20s, followed by high-resolution melting. Each sample was run in triplicate. Housekeeping gene ef1a was used as a reference gene, using primers ef1a-f (5'-TGGTACTTCTCAGGCTGACT-3') and ef1a-r (5'TGACTCCAACGATCAGCTGT-3'). The delta-delta CT method was used to quantify expression levels. All values were normalised to wildtypes to provide the relative expression of the gene of interest.

Transmission electron microscopy

Larval tissue was prepared for TEM using the microwave fixation protocol as previously described (Czopka and Lyons, 2011; Karttunen et al., 2017). For adult tissue, adult zebrafish were terminally anaesthetised in tricaine and perfused intracardially with PBS followed by primary fixative solution (4% paraformaldehyde, 2.5% glutaraldehyde, 0.1M sodium cacodylate) (Sigma Aldrich). Adults were subsequently incubated in fresh primary fixative solution for 24 hours at 4ºC. Spinal cords were dissected and processed using the microwave fixation protocol described for larval tissue. TEM images were obtained using a JEOL JEM-1400 Plus Electron Microscope. Image magnification ranged from 11.2-17kx magnification for larval spinal cords, and 1.7kx for adult spinal cord.

Single cell labelling

Fertilised eggs from *myrf*^{ue70} heterozygous adult in-crosses were microinjected between the single and four-cell stage with 10ng/µl plasmid DNA encoding mbp:mCherry-CAAX (Mensch et al., 2015) and 25ng/µl tol2 transposase mRNA in nuclease free water with 10% phenol red. Animals were screened at 4 dpf for mosaically labelled oligodendrocytes and subsequently imaged. Isolated single cells from any level in the dorsal spinal cord were imaged. Images were obtained in 4 and 6 dpf larvae.

Live imaging

Larvae were anaesthetised in tricaine/MS-222 (ethyl3-aminobenzoate methanesulfonate salt, Sigma Aldrich) in HEPES buffered E3 embryo medium and embedded in 1.3-1.5% low melting point agarose (Invitrogen). All fluorescent images were acquired using a Zeiss LSM 880 confocal microscope with a 20x objective (Zeiss Plan-Apochromat 20x dry, NA = 0.8, Carl Zeiss Microscopy). Z-stacks were obtained through the entire single cell, axon or spinal cord according to each experiment. For time course imaging, a single oligodendrocyte was imaged as at 4 dpf. Larvae were then extracted from agarose gel, recovered in embryo medium and maintained with daily feeds and water exchange until imaging of the same cell was repeated at 6 dpf. For automated imaging of the entire spinal cord and peripheral nervous system, Vertebrate Automated Screening Technology (VAST) was utilised as described previously (Early et al., 2018). Briefly, larvae are arrayed into individual wells of a 96-well plate containing MS-222 treated HEPES buffered E3 embryo media. Fish are loaded and oriented for imaging using a Large Particle (LP) Sampler and VAST BioImager system (Union Biometrica Inc)

fitted with a 600µm capillary tube. Embryos are automatically loaded into the capillary, positioned and imaged using an AxioCam 506m CCD Camera, a CSU-X1 spinning disk confocal scanner, a 527/54+645/60nm double bandpass emission filter, 1.6x C-Mount adapter, a PIFOC P-725.4CD piezo objective scanner, W-Plan-Apochromat 10x 0.5NA objective and an Axio Examiner D1. Z-stacks covering the depth of the capillary were acquired using a 4µm z-interval, 3x3 binning and 60ms exposure. Images were acquired using brightfield and the appropriate fluorescent channel. Following imaging, larvae were dispensed into a corresponding well of a 96-well collection plate and whole tissue retained for genotyping. Unless otherwise stated, all confocal images presented in this manuscript represent a lateral view of the zebrafish spinal cord, with anterior to the left and posterior to the right, and dorsal/ventral at the top/bottom of the image respectively. Within experiments, images were obtained using similar laser intensity and optical gain settings. All imaging was performed blinded to genotype.

Transmission electron microscopy

TEM images were tiled using the automated photo merge tool in Adobe Photoshop 2019. The number of ensheathed axons was counted in one hemi-spinal cord section per larva using the cell counter tool in FIJI ImageJ. Axon caliber is defined as the area of the axon within this manuscript. Axonal area was calculated using the freehand line and measure tool in FIJI ImageJ. A g-ratio represents the ratio between the inner and outer diameter of the myelin sheath (i.e. a larger g-ratio values denotes a thinner myelin sheath). This calculation assumed perfect circularity of axons, which is not true to larval zebrafish TEM preparations. Thus, within these experiments g-ratio was calculated by dividing axonal area by the axonal + associated myelin area.

VAST

Images obtained using VAST were stitched and processed using FIJI ImageJ software (Schindelin et al., 2012) and custom macros (Early et al., 2018). Semi-automated oligodendrocyte counts were performed on the maximum intensity projection images (Early et al., 2018). Cell count values represent all oligodendrocytes in the spinal cord (dorsal and ventral tracts). Morphometric analysis of larval developmental features was performed on brightfield images. Measurements of ocular diameter, body length and swim bladder height were performed using the line and measure tool in FIJI ImageJ (National Institutes of Health).

Single cell imaging

Confocal z-stack images were airyscan processed using Zen software (ZEISS). Images were opened in FIJI ImageJ. Cells were included for analysis only if all myelin sheaths were distinguishable. Myelin sheath lengths were measured using the freehand line and measure tools. Myelin sheath number was equivalent to the number of measurements performed. Total myelin per cell was calculated as sum of all myelin sheaths lengths per cell. Abnormal sheaths were defined at sheaths with abnormal elongation profiles, incomplete wrapping or myelin blebbing. For time course experiments, net growth or shrinkage of myelin sheaths was calculated as the average myelin sheath length at 6 dpf minus the average myelin sheath length at 4 dpf. Where possible, all myelin sheaths per cell were measured. In instances where measurement of all myelin sheaths was not possible (due to other cells coming into close proximity), only isolated myelin sheaths were analysed at each time point. The number of retracted sheaths was recorded, and these sheaths were excluded from sheath growth analysis.

Electrophysiology

Zebrafish were dissected as described previously in Roy & Ali (2013) to access the Mauthner neuron. In short, 6 dpf anaesthetised zebrafish were laid on their sides on a Sylgard dish and secured using tungsten pins through their notochords in a dissection solution containing the following (in mM): 134 NaCl, 2.9 KCl, 2.1 $CaCl_2$, 1.2 $MgCl_2$, 10 HEPES, 10 glucose and 160mg/ml tricaine, adjusted to pH 7.8 with NaOH. Their eyes as well as lower and upper jaws were removed using forceps to expose the ventral surface of the hindbrain, which was secured with an additional tungsten pin. The motor neurons in the anterior spinal cord were exposed as described by Wen et al (2005). A dissecting tungsten pin was used to remove the skin and the muscle overlaying the motor neurons in a single segment. Following the dissection, zebrafish together with their recording chamber were moved to the rig and washed with extracellular solution containing the following (in mM): 134 NaCl, 2.9 KCl, 2.1 $CaCl_2$, 1.2 $MgCl_2$, 10 HEPES and 10 glucose with 15 μM tubocurarine. The cells were visualised using Olympus microscope capable of DIC using 60X water immersion NA = 1 objective lens and Rolera Bolt Scientific camera with Q-Capture Pro 7 software. The stimulating electrode filled with extracellular solution was then positioned in the mid spinal cord lightly touching the exposed neurons underneath. Mauthner whole-cell recordings were performed with thick-walled borosilicate glass pipettes pulled to 6–10 MΩ. The internal solution contained the following (in mM): 25 K-gluconate, 15 KCl, 10 HEPES, 5 EGTA, 2 $MgCl_2$, 0.4 NaGTP, 2 Na_2ATP, and 10 Na-phosphocreatine, adjusted to pH 7.4 with KOH. Upon formation of whole-cell patch clamp, 270s – long recording was performed in the current - clamp configuration. Cell resting membrane potential was established as an average of the first 5 seconds of the recording if the cell did not fire during that

time. To measure the conduction velocity along the Mauthner axon, the zebrafish were washed with recording solution containing the following (in mM): 134 NaCl, 2.9 KCl, 2.1 $CaCl_2$, 1.2 $MgCl_2$, 10 HEPES and 10 glucose with addition of (in μM) 50 AP5, 20 strychnine, 100 picrotoxin and 50 CNQX. The antidromic Mauthner action potentials were recorded following the field stimulation by the stimulating electrode connected to DS2A Isolated Voltage Stimulator (Digitimer) in the spinal cord. 30 consecutive action potentials were recoded every 5 seconds using Clampex 10.7 at 100kHz sampling rate and filtered at 2 kHz using MultiClamp 700B. At the end of the recording, images of the zebrafish were obtained with 4X objective and stitched using Adobe Photoshop. The resulting image was then transferred to FIJI and the distance between stimulating and the recording electrode was measured. The conduction velocity of action potential was calculated dividing the distance between the electrodes by the latency from the stimulus artefact to the peak of action potential. Action potential latency and half-width were measured using homebuilt MATLAB script. For the analysis of action potential fidelity consecutive trains of 10 stimuli were delivered at 1, 10, 100, 300, 500 and 1000Hz every 30s. Recordings were made at 20kHz sampling rate and filtered at 2 kHz. The number of action potentials were calculated using Clampfit 10.7 software and the action potential success rate was calculated as a number of action potentials fired out of 10 and multiplied by 100.

Behavioural assay

Analysis of startle behaviour in 5-6 dpf *myrf*^{ue70} mutant and wildtype larvae was performed as previously described (Burgess and Granato, 2007a, Wolman et al, 2011). Briefly, larvae were placed into individual wells of a 6 x 6 custom made acrylic testing plate containing E3 embryo media. A series of 10 acoustic stimuli (40.6 dB, 1000 Hz, 3ms duration) were delivered to the plate with an interstimulus interval of 20 seconds. Behaviour was recorded using a high-speed camera (Photron Fastcam Mini UX) at 1000frames/s. Analysis of recorded video footage was performed using FLOTE v2.0 tracking software (Burgess and Granato 2007a). Larvae that responded to less than 70% of the stimuli were excluded from further kinematic analysis. Average behavioural latency was calculated as an average per larva over all behavioural responses. Short latency C-starts (SLC) and long latency C-starts (LLC) were defined by identifying a latency value (16ms) separating the two peaks of the latency bimodal distribution in wildtype *myrf*^{ue70} larvae. Behavioural latency, c-bend duration, initial turn angle, and angular velocity for SLC and LLC events were defined and analysed as previously described (Burgess and Granato, 2007a).

Experimental design and statistical analysis

Unless stated otherwise, all experiments were performed on 6 dpf larvae from adult heterozygous in-crosses. All subjects were the offspring of third generation, or younger, adults. The experimenter was blinded to the genotype of the larvae during all experiments and analysis. The sex of the animals was unknown as sex specification has not occurred at this stage of larval development. All graphs and statistical testing were performed using GraphPad Prism. All data was assessed for Gaussian distribution using a D'agostino Pearson omnibus normality test. Parametric continuous data was analysed using a two-tailed unpaired student's t test, or two-way ANOVA, according to the number of variables being compared. Non-parametric continuous data was analysed using a Mann-Whitney test. If the number of values were too small to assess for normality, it was assumed that data was non-parametric. Results were considered statistically significant when $p < 0.05$. Within figures, p values are denoted as follows: non-significant i.e. $p > 0.05$ 'ns', $p < 0.05$ '*', $p < 0.01$ '**', $p < 0.001$ '***', $p < 0.0001$ '****'. Unless otherwise stated, all data was averaged per biological replicate (N represents number of larvae). Throughout the figures, error bars represent mean ± standard deviation for parametric data, or median and interquartile range for non-parametric data. Details of statistical tests, precise p and n values for each experiment are provided in the appropriate figure legends.

Code accessibility

Custom written code to perform automated cell counts is available in a previous publication (Early et al., 2018). Code to interpret electrophysiological data is available at https://github.com/skotuke/Mauthner_analysis.

Results

Targeting myelin gene regulatory factor to create a larval zebrafish model of CNS-specific hypomyelination

To begin our investigations into the role of CNS myelination in neural circuit function, we sought to establish a larval zebrafish model with CNS-specific hypomyelination. Mammalian studies have identified myelin gene regulatory factor (myrf) as a transcription factor vital for CNS myelin formation and maintenance (Bujalka et al., 2013; Emery et al., 2009). Zebrafish possess a single ortholog of myrf and, similar to mammals, myrf expression in the CNS appears to be restricted to oligodendrocytes (Klingseisen et al., 2019; Treichel and Hines, 2018). We used CRISPR/Cas9 technology to target a guide RNA to exon 2 of the zebrafish myrf gene, the first conserved exon across all predicted splice variant isoforms, and in doing so created the *myrf*^{ue70} mutant (Methods and **Figure 1A).** Morphometric analysis of larval body features of *myrf*^{ue70} mutants at larval stages showed them to be indistinguishable from siblings (data not shown), and in contrast to mammalian myrf mutants (Emery et al., 2009), homozygous *myrf*^{ue70} mutants remain viable through to adulthood. Adult *myrf*^{ue70} mutants exhibited an almost complete absence of *mbp* mRNA (**Figure 1B**), and transmission electron microscopy (TEM) assessment indicated effectively no myelin in the adult spinal cord **(Figure 1C and D).** In addition, and unlike larvae, homozygous adult *myrf*^{ue70} were grossly identifiable from their siblings by their smaller size. Adult *myrf*^{ue70} mutants were also infertile, due to the absence of detectable gonadal tissue in females, confirmed via histopathology, which also revealed evidence of cardiomyopathy (data not shown) - findings consistent with proposed roles of myrf outside the CNS (Hamanaka et al., 2019; Pinz et al., 2018; Rossetti et al., 2019).

Given the potential to study myelination of well-defined circuits at high resolution over time at larval stages when *myrf*^{ue70} mutants are morphologically indistinguishable from siblings, we next analysed our transgenic reporter of myelination Tg(mbp:eGFP-CAAX) at 6 days post fertilisation (dpf). This indicated that the gross level of CNS myelination was also reduced in *myrf*^{ue70} mutant larvae relative to wildtype siblings (**Figure 1E**). To quantify myelination in larvae, TEM was performed on transverse sections of the spinal cord (CNS) and posterior lateral line nerve of the peripheral nervous system (PNS) at 6 dpf (**Figure 2A-C)**. At this timepoint, we observed a 66% reduction in the number of myelinated axons in the spinal cord of *myrf*^{ue70} mutants relative to wildtype siblings (35.29 ± 7.83 myelinated axons in wildtypes, 12.00 ± 4.34 myelinated axons in mutants, $p \leq 0.0001$, unpaired t-test) (**Figure 2D**). In contrast, and demonstrating specificity of

hypomyelination to the CNS, similar numbers of myelinated axons were observed in the PNS of mutant and wildtype siblings (7.33 ± 1.53 myelinated axons in wildtypes, 9.00 ± 3.83 myelinated axons in mutants, p = 0.52, unpaired t-test) (**Figure 2E**).

Despite the large number of unmyelinated axons in *myrf*^{ue70} mutants, our TEM analyses indicated that some axons remained ensheathed in the larval CNS, including the very large diameter Mauthner axons, the first reticulospinal axons to be myelinated in the zebrafish CNS (Almeida et al., 2011). Although Mauthner axons were ensheathed in *myrf*^{ue70} mutants at 6 dpf, they had significantly thinner myelin sheaths compared to wildtype siblings (average g-ratio: 0.48 ± 0.009 in wildtypes, 0.80 ± 0.08 in homozygous mutants, p = 0.0009, unpaired t-test, **Figure 2F**). A similar finding was observed in the other axons that were ensheathed in *myrf*^{ue70} mutants at this stage, with greater g-ratio values (denoting thinner myelin) for other large caliber (>0.3μm^2) axons in mutants than in wildtype siblings (average g-ratio: 0.60 ± 0.08 wildtypes, 0.71 ± 0.08 mutants, p ≤0.0001, unpaired t test, **Figure 2G**). Despite the generally severe hypomyelination phenotype, the presence of some large caliber myelinated axons in zebrafish *myrf*^{ue70} mutants at larval stages contrasts with our analysis of adult zebrafish mutants and myrf mutant mice which both have essentially a complete absence of CNS myelination (Emery et al., 2009). This suggests that the full effects of myrf knockout may be masked at early stages, either by maternal gene expression or genetic compensatory mechanisms (Rossi et al., 2015).

To examine the cellular basis of CNS hypomyelination in *myrf*^{ue70} mutant larvae, we first assessed myelinating oligodendrocyte number using the transgenic reporter Tg(mbp:nls-eGFP) (Karttunen et al., 2017) (**Figure 3A**). At 6 dpf, the timepoint at which TEM was performed, the number of detectable oligodendrocytes was reduced by 21% in *myrf*^{ue70} mutants relative to wildtype siblings (p = 0.0002, unpaired t-test, **Figure 3B)**. In addition, the fluorescent intensity of *myrf*^{ue70} mutant oligodendrocyte nuclei was reduced, consistent with reduced *mbp* expression. Because, the reduction in cell number was not sufficient to explain the reduction in myelin observed using TEM, we assessed the morphology of individual myelinating oligodendrocytes using mosaic cell labelling with the mbp:mCherry-CAAX reporter construct (Almeida et al., 2011) (**Figure 3C**). We found that both myelin sheath number (p = 0.02, Mann Whitney test, **Figure 3D**) and length (p = 0.002, unpaired t test, **Figure 3E**) were reduced in *myrf*^{ue70} mutants by 33% and 25% respectively at 6 dpf, with total myelin (sum of sheath lengths) per individual oligodendrocyte reduced by 47% in mutants relative to wildtypes (p ≤ 0.0001, unpaired t test, **Figure 3F**). In addition to being required for the initiation of myelination, previous studies in rodents indicate that myrf is also essential for myelin sheath maintenance (Koenning et al., 2012). Having observed that adult *myrf*^{ue70} mutants have a much more severe hypomyelination phenotype than larvae

(**Figure 1D**), we wanted to assess how the morphology of single oligodendrocytes changed over time. To do so, we imaged single oligodendrocytes at 4 dpf and again at 6 dpf (**Figure 3G**). We found that between these timepoints mutant oligodendrocytes demonstrated a net shrinkage in myelin sheath length, while wildtype oligodendrocytes showed a net growth ($p = 0.009$, Mann Whitney test, **Figure 3H**). Furthermore, the number of myelin sheaths that were completely retracted during this timeframe was significantly higher in *myrf*^{ue70} mutant oligodendrocytes ($p = 0.003$, unpaired t test, **Figure 3I).** Also consistent with a failure to maintain healthy myelin sheaths, the number of myelin sheaths exhibiting an abnormal morphology (i.e. incomplete wrapping, abnormal elongation profiles or myelin blebs) was significantly higher in mutant versus wildtype oligodendrocytes at 6 dpf (**Figure 3J).**

In summary, disrupting myrf leads to a CNS-specific hypomyelination phenotype in larval zebrafish, caused by a reduction in the number of oligodendrocytes, with those that remain having fewer and shorter sheaths. The majority of sheaths that are made are thinner, and, based on our documentation of almost complete absence of myelin in adults, not maintained long-term. Therefore, the phenotype in the *myrf*^{ue70} mutant fulfilled our aim to generate a CNS-specific model of hypomyelination to study the effects on neural circuit function at larval stages.

myrf^{ue70} mutants exhibit an increase in the latency to perform startle responses and an impaired behavioural choice in response to a defined auditory stimulus

Given that many larval zebrafish sensorimotor behaviours are mediated by RS neurons, whose axons are myelinated early and exhibit activity-regulated myelination (Koudelka et al., 2016), we hypothesised that *myrf*^{ue70} mutants would display detectable differences in the performance of RS-mediated behaviours. To test this, we chose to first examine acoustic-startle behaviour, for which the underlying circuit is relatively well described (Hale et al., 2016). Briefly, a high-intensity acoustic stimulus activates the auditory (VIIIth) nerve, which courses into the hindbrain to synapse onto the Mauthner cell at its lateral dendrite. Once the threshold potential is exceeded, an action potential is elicited and rapidly propagated along the Mauthner axon, which crosses into, and extends along, the contralateral tract of the spinal cord. Along its length, collateral branches make synapses with interneurons and primary motor neurons that coordinate motor output. Activation of a Mauthner axon results in a stereotypical, high-velocity 'c-bend' away from the stimulus, followed by a fast burst swim (Kimmel et al., 1974) (**Figure 4A**). The latency to perform such a response is defined as the time taken from stimulus presentation to the onset of a c-bend (**Figure 4J**). Given that myelin increases conduction

velocity along a single axon (Waxman, 1980), we made the prediction that the latency to execute the motor responses following an acoustic stimulus would be delayed in *myrf*^{ue70} mutants.

Motor behaviour was assessed using an established high-throughput assay (Burgess and Granato, 2007a). *myrf*^{ue70} larvae were arrayed into individual wells of a 6x6 custom made plate attached to an amplifier delivering a series of acoustic stimuli at 20 second intervals (**Figure 4B**). Using a high-speed (1000Hz) camera, behavioural responses were recorded and subsequently analysed using FLOTE software (Burgess and Granato, 2007a, 2007b). Overall, the frequency of responses to acoustic stimuli was similar between groups **(Figure 4E).** However, on average, *myrf*^{ue70} mutants exhibited a 66% increase in their average latency to elicit a response compared to wildtype siblings (wildtypes: 10.55ms (9.6-16.16ms), mutants: 17.60ms (12.90-21.88ms), $p = 0.003$, Mann Whitney Test, **Figure 4F)**.

Interestingly, larval behavioural responses to acoustic stimuli can be modulated across variable stimulus properties, exhibiting decision-making capabilities of the underlying circuitry (Burgess and Granato, 2007a; Jain et al., 2018). For example, in larval zebrafish, while high intensity threatening stimuli induce the short-latency c-bend startle response, also known as the 'short latency c-start' (SLC), lower stimulus intensities induce a distinct longer latency reorientation-like behaviour, initially defined as a 'long latency c-start' (LLC). These kinematically and behaviourally distinct responses are executed by activity in partially overlapping circuitry, with the crucial difference that SLCs are driven by recruitment of Mauthner neurons, while LLCs appear to be driven by alternative pathways e.g. prepontine neurons (Burgess and Granato, 2007a; Marquart et al., 2019) (**Figure 4A**). Given that hypomyelination in *myrf*^{ue70} is widespread within the CNS, we anticipated that the large overall increase in latency to respond to acoustic stimuli might be due to significant delays in the performance of both SLC and LLC responses. However, when data was segmented into SLCs or LLCs, the latency to perform an SLC was increased by 6.4% (10.03 ± 0.85ms in wildtypes, 10.67 ± 0.83ms in mutants, $p = 0.006$, unpaired t test **Figure 4G and I**), but the latency to perform LLCs remained unaffected **(Figure 4H and I)**, begging the question as to what caused the much larger overall increase in latencies to respond to acoustic stimuli.

We reasoned that if the latency to perform SLCs was only affected to a small degree and LLCs not at all, the overall large increase in latency to perform all responses might be due to a biased selection of the longer latency LLCs over the much shorter latency SLCs. Indeed, when we compared their relative frequency, we saw that LLCs represented a significantly increased proportion of behavioural responses in *myrf*^{ue70} mutants relative to wildtypes (SLC:LLC ratio: 10:1 in wildtypes, 2.9:1 in mutants, $p \leq 0.0001$, Kolmogorov-Smirnov test,

Figure 4C and D). To ensure that this apparent bias in behavioural selection was not due to SLCs simply being so slow as to be detected as LLCs, we analysed additional kinematic parameters (**Figure 4J-N**), which have specific values associated with each type of response (Burgess and Granato, 2007a). No differences were found in the duration, maximum angular velocity or initial turning angle of SLCs or LLCs between wildtype and mutant larvae (**Figure 4K-M**), consistent with the conclusion that the increased frequency of LLCs represents true LLC events, rather than delayed and inappropriately classified SLCs.

In summary, we have shown that *myrf*^{ue70} mutants exhibited delayed latency to perform Mauthner-mediated startle responses (SLCs), and an unexpected bias towards performing Mauthner-independent reorientation behaviours (LLCs) in response to the same acoustic stimuli. This shows that hypomyelination in the larval zebrafish can be detected in overt changes to behaviour and highlights the complexity of how dysregulation of myelination impacts circuit function, even when executing relatively simple sensorimotor transformations.

Action potential conduction is impaired along the Mauthner axon in *myrf*^{ue70} mutants

In order to investigate how myelination affects conduction along larval zebrafish axons, we set out to establish an electrophysiological platform that would allow us to measure and compare multiple aspects of axonal conduction in vivo. We focussed our analysis on the Mauthner neuron and axon, due to its characteristic morphology and anatomical location, and given its established role in mediating the SLC. To begin with, we performed whole-cell current-clamp recordings of the Mauthner neuron cell body while stimulating its axon in the spinal cord with an extracellular electrode (**Figure 5A).** We first tested whether loss of *myrf* function affected intrinsic properties of the Mauthner neuron, by assessing its resting membrane potential: we found that this remained stable in mutants (siblings: -70.82 ± 2.76mV, mutants: -70.68 ± 1.25mV, p = 0.9077, unpaired t-test**, Figure 5B**). Our experimental configuration allowed us to record antidromic action potentials propagating along the Mauthner axon. Therefore, we next assessed whether the shape of action potentials was disrupted by hypomyelination, by measuring the width of the action potential at its half-height (action potential half-width) at 6 dpf, which we found to be similar in control and *myrf*^{ue70} mutant animals (siblings: 0.64 ± 0.09ms, *myrf*^{ue70} mutants: 0.60 ± 0.06ms, p = 0.2610, unpaired t-test, **Figure 5C and D**). These data indicate that the degree of hypomyelination along Mauthner axons in *myrf*^{ue70} mutants at these stages does not affect the Mauthner resting membrane potential or greatly affect the shape of the action potentials.

Given the well-defined role for myelin in speeding-up action potential conduction, and the evidence of an increased latency to perform the Mauthner-dependent SLC response, we next measured the latency of action potential conduction along the Mauthner axon in controls and *myrf*^{ue70} mutants. This analysis showed that the normalised latency of action potentials was significantly increased in *myrf*^{ue70} mutants when compared to siblings (siblings: 0.80 ± 0.11ms/mm, mutants: 0.97 ± 0.07ms/mm, p = 0.0003, **Figure 5F**) resulting in an 18% reduction in conduction velocity (siblings: 1.27 ± 0.17m/s, mutants: 1.04 ± 0.08m/s, p = 0.0005, **Figure 5G).** This reduction in conduction velocity supports our finding of a delayed execution of SLCs in *myrf*^{ue70} mutants. We next assessed whether the precision of action potential propagation might be impaired due to hypomyelination, which might interfere with synaptic signalling in the circuit. To do so, we measured the 'jitter', or imprecision, in the timing of action potential arrival following stimulation, as the standard deviation of 30 action potential peak times aligned to the stimulus artefact (**Figure 5H**). No differences were observed in the precision of action potential arrival in *myrf*^{ue70} mutants at 6 dpf (siblings: 0.006 ± 0.002ms, mutants: 0.006 ± 0.0009ms, p = 0.8166, unpaired t-test, **Figure 5I**). These data suggest that hypomyelination leads to slower, but nonetheless precise, action potential propagation.

Given that the action potentials conducted along Mauthner axons in *myrf* mutants are likely to be sufficient to trigger downstream motor output, albeit with a longer delay, we next asked whether the hypomyelination of Mauthner axon might lead to an increased failure to reliably propagate action potentials. Therefore, we implemented a strategy to robustly test the ability of the myelinated axon to faithfully transmit action potentials. With our preparation, we observed that the Mauthner cell could spontaneously fire short trains of action potentials (1-10) at high frequency (~300Hz) while in the resting state, prior to our adding pharmacological reagents to block network-level input on to Mauthner and ahead of taking control of stimulating activity in the preparation, for the analyses noted above (data not shown). On the basis of this observation, and given the evidence from studies in rats that dysmyelination can influence firing frequency (Kim et al., 2013) we established a high-frequency stimulation paradigm to assess how hypomyelination affected the ability of the Mauthner axon to sustain high frequency firing of action potentials. To do so, we used our field stimulation procedure and delivered 10 stimuli at various frequencies via the stimulating electrode and recorded the number of action potentials fired by the Mauthner cell, which allowed us to assess action potential success rate (**Figure 5J**).Given that myelination reduces axonal current leakage, we predicted that our high frequency stimulation protocol may reveal failed action potential propagation. When we analysed the success rate of action potential firing, we found that this was indistinguishable between siblings and mutants at 300Hz,

insignificantly different at 500Hz, but significantly impaired at 1000Hz stimulation, where we found that Mauthner cells from mutants fired with a significantly lower success rate (siblings: 55.79 ± 10.17%, mutants: 38.89 ± 17.64%, p = 0.0014, two-way ANOVA, **Figure 5K)**. This assay suggests that hypomyelination impairs the ability of axons to propagate action potentials faithfully, which could contribute to the behavioural shift away from Mauthner-mediated responses to auditory stimuli.

In conclusion, we have established an electrophysiology platform that allows direct measurement of single cell (i.e. Mauthner) conduction properties in vivo. In doing so, we have demonstrated that hypomyelination of the Mauthner axon leads to slowed conduction velocity, and with a high frequency stimulation paradigm we reveal a loss of fidelity of action potential propagation along the hypomyelinated Mauthner axon.

Discussion

We have demonstrated that CNS hypomyelination leads to behavioural alterations and impaired conduction along axons in larval zebrafish. We found that *myrf*^{ue70} mutant zebrafish larvae exhibit CNS-specific hypomyelination, representing the first model with which one can study the role of CNS myelin in behaviour. These mutants exhibited an increased latency to execute the stereotypical rapid acoustic startle responses (SLCs) and were also biased towards performing longer latency reorientation behaviours (LLCs) in response to startle-inducing acoustic stimuli. The fact that our analysis revealed phenotypes in both the speed of executing a specific behaviour and in the selection of the correct behavioural response to a sensory stimulus indicates the complex roles that myelination plays in regulating circuit function. These findings provide encouragement that studying additional behaviours will offer further entry-points into studying how alterations to myelination affect the function of other neural circuits. Indeed, there are now a large number of behavioural paradigms that allow analysis of larval zebrafish circuit function, from various sensorimotor transformations (Dunn et al., 2016; Henriques et al., 2019; Naumann et al., 2016), behaviours regulated by sensory experience over time (Burgess and Granato, 2007a; Wolman et al., 2011) and those driven by inter-individual interactions, such as sociability (Dreosti et al., 2015; Larsch and Baier, 2018).

In addition to studying behaviour, we established electrophysiological protocols to assess the conduction properties of single neurons and axons, focusing on the Mauthner neuron due to the ease of its identification and its involvement in the acoustic startle response. We found that conduction along the

hypomyelinated Mauthner axon was reduced, and that Mauthner axons in *myrf*^{ue70} mutants exhibited an increased failure to propagate action potentials in response to high-frequency stimulation. It remains to be determined precisely how disruption to the conduction properties of neurons and axons caused by hypomyelination affects circuit function and behavioural outputs. For example, the slowed execution of the SLC may be due to more than the slower conduction along the hypomyelinated Mauthner axon of myrf mutants, including slower conduction elsewhere in the circuit. Precisely how hypomyelination leads to a biased recruitment of LLCs over SLCs in response to the same auditory cue in *myrf*^{ue70} mutants also remains to be elucidated, but could be influenced by the impaired ability to sustain high frequency firing along the hypomyelinated Mauthner axons, and dysregulated recruitment of downstream motor pools. However, with our antidromic preparation, we cannot rule out the possibility that the reduced success rate of high frequency action potential conduction was influenced by impaired generation of action potentials in the axon. Therefore, establishing methods to record orthodromic action potentials remains an important challenge for the future. In addition, to study how dysregulation of myelination influences synaptic signalling, electrophysiological analyses through the paired recordings of neurons known to communicate within circuits will be required. These studies, alongside the ability to assess the conduction properties of additional neurons, will be required to generate complete circuit models of how myelin influences even simple behaviours. Our study documented behavioural alteration and disruption to conduction in larvae with CNS-specific hypomyelination, but many challenges remain in integrating our understanding of circuit function across scales from conduction and synaptic communication through population-level neuronal activity and the execution of specific behaviours. However, we believe that the zebrafish represents a model in which such a multi-scale analyses of myelination on neural circuit function is feasible.

The larval zebrafish has numerous advantages that facilitate analyses of circuit function across scales. The larval CNS is relatively simple compared to mammalian models; with approximately one hundred thousand neurons by 6 dpf, only a relatively small proportion (on the order of a few hundred neurons) have myelinated axons at this stage (Hildebrand et al., 2017). The myelination of those axons is generally very stereotyped, with myelination of certain neuronal subtypes (e.g. reticulospinal neurons) adaptable and responsive to neuronal activity (Koudelka et al., 2016). With the aim of studying myelination from the perspective of neural circuits, we previously developed tools to study patterns of myelination along single axons in vivo (Koudelka et al., 2016). These tools, together with increasing availability of neuron-specific drivers coupled with circuit maps of

the larval fish brain provide a great opportunity to map myelination at single cell resolution across the larval zebrafish CNS, and to do so over time. Even with myelination patterns mapped, a corresponding challenge will be to manipulate myelin from the point of view of specific neurons/axons and circuits. As noted above, it remains unclear whether the longer latency to execute the startle response is simply due to hypomyelination of Mauthner axons, or elsewhere in the circuit, and it may even be influenced by complex integrative functions that affect timing across the circuit. Therefore, it will be important to develop methods to regulate myelination in a neuron/axon and circuit-specific manner. One possibility might be to selectively ablate oligodendrocytes in specific circuits. Although oligodendrocyte ablation can be carried out at single cell resolution in zebrafish larvae (Auer et al., 2018), it leads to inflammatory reactions by cells such as microglia (Karttunen et al., 2017), which may be relevant to disease contexts, but would confound the disentangling of the role of myelin per se in healthy circuits. Therefore, an additional approach might be to express cell surface proteins that inhibit myelination (Redmond et al., 2016) along the axons of specific neuronal cell types (Burgess et al., 2009; Tabor et al., 2018; Yamanaka et al., 2013), selectively preventing their myelination. Furthermore, as signals and receptors that influence adaptive activity-regulated myelination are identified, yet more strategies to influence myelination in localised manners may emerge.

In addition to needing more refined methods to map and manipulate myelination of specific circuits, additional tools to assess function across scales from single axon to behaving animal will be required. Given the challenges of integrating complex electrophysiological protocols with behavioural observation in small zebrafish larvae, it is possible that optical methods to assess function across scales provides a better opportunity to bridge analyses across scales. Indeed, optical imaging approaches have already proven hugely powerful in the study of larval zebrafish brain function. For example, two-photon and light-sheet microscopy-based imaging studies allow the analysis of the activity of individual neurons (Abdelfattah et al., 2019) through to sampling the activity of effectively all neurons the entire larval zebrafish brain, at multiple volumes per second with sub-cellular resolution (Ahrens et al., 2013, 2012; Chen et al., 2018). In fact, sophisticated imaging platforms that allow monitoring of neuronal activity in the brain during the execution of behaviours have been developed, including during acoustic stimulus-driven responses (Jain et al., 2018; Lacoste et al., 2015). Furthermore, the coordinated activity of ensembles of neurons have been investigated in the larval brain, which provides an opportunity to investigate how potentially even subtle alterations to myelination in development, health or disease might influence relatively high-order network activity (Diana et al., 2018; Romano et al., 2015; Sumbre et al., 2008; Wolf et al., 2017). To date, most optical analyses of neuronal activity in zebrafish have been carried

573 out using genetically encoded Ca^{2+} reporters, but the limited temporal kinetics of even the fastest Ca^{2+} reporters
574 may preclude the analysis of millisecond-scale changes to conduction properties, which our data indicate can be
575 expected with disruption to larval myelination. However, ongoing development and refinement of voltage
576 indicators appear to exhibit photodynamic properties with the sensitivity to detect functional changes to
577 conduction and synaptic properties at the appropriate temporal resolution, including in larval zebrafish
578 (Abdelfattah et al., 2019). Employing indicators that allow bona fide assessment of conduction in the intact
579 brain, during the execution of behaviours has the potential to provide a transformative capacity to interrogate
580 how myelin influences circuit function.

581 In summary, our study presents larval zebrafish as a viable model to study myelination across scales
582 from molecular and cellular analyses of how myelin organises and supports axons through to functional
583 assessments of conduction, synaptic communication, network function and behaviour over time.

References:

Abdelfattah, A.S., Kawashima, T., Singh, A., Novak, O., Liu, H., Shuai, Y., Huang, Y.-C., Campagnola, L., Seeman, S.C., Yu, J., Zheng, J., Grimm, J.B., Patel, R., Friedrich, J., Mensh, B.D., Paninski, L., Macklin, J.J., Murphy, G.J., Podgorski, K., Lin, B.-J., Chen, T.-W., Turner, G.C., Liu, Z., Koyama, M., Svoboda, K., Ahrens, M.B., Lavis, L.D., Schreiter, E.R., 2019. Bright and photostable chemigenetic indicators for extended in vivo voltage imaging. Science eaav6416. https://doi.org/10.1126/science.aav6416

Ahrens, M.B., Li, J.M., Orger, M.B., Robson, D.N., Schier, A.F., Engert, F., Portugues, R., 2012. Brain-wide neuronal dynamics during motor adaptation in zebrafish. Nature 485, 471–477. https://doi.org/10.1038/nature11057

Ahrens, M.B., Orger, M.B., Robson, D.N., Li, J.M., Keller, P.J., 2013. Whole-brain functional imaging at cellular resolution using light-sheet microscopy. Nat. Methods 10, 413–420. https://doi.org/10.1038/nmeth.2434

Almeida, R.G., 2018. The Rules of Attraction in Central Nervous System Myelination. Front. Cell. Neurosci. 12, 367. https://doi.org/10.3389/fncel.2018.00367

Almeida, R.G., Czopka, T., ffrench-Constant, C., Lyons, D.A., 2011. Individual axons regulate the myelinating potential of single oligodendrocytes in vivo. Development 138, 4443–4450. https://doi.org/10.1242/dev.071001

Auer, F., Vagionitis, S., Czopka, T., 2018. Evidence for Myelin Sheath Remodeling in the CNS Revealed by In Vivo Imaging. Curr. Biol. 28, 549-559.e3. https://doi.org/10.1016/j.cub.2018.01.017

Bonnefil, V., Dietz, K., Amatruda, M., Wentling, M., Aubry, A.V., Dupree, J.L., Temple, G., Park, H.-J., Burghardt, N.S., Casaccia, P., Liu, J., 2019. Region-specific myelin differences define behavioral consequences of chronic social defeat stress in mice. eLife 8, e40855. https://doi.org/10.7554/eLife.40855

Bujalka, H., Koenning, M., Jackson, S., Perreau, V.M., Pope, B., Hay, C.M., Mitew, S., Hill, A.F., Lu, Q.R., Wegner, M., Srinivasan, R., Svaren, J., Willingham, M., Barres, B.A., Emery, B., 2013. MYRF Is a Membrane-Associated Transcription Factor That Autoproteolytically Cleaves to Directly Activate Myelin Genes. PLoS Biol. 11, e1001625. https://doi.org/10.1371/journal.pbio.1001625

Burgess, H.A., Granato, M., 2007a. Sensorimotor Gating in Larval Zebrafish. J. Neurosci. 27, 4984–4994. https://doi.org/10.1523/JNEUROSCI.0615-07.2007

614 Burgess, H.A., Granato, M., 2007b. Modulation of locomotor activity in larval zebrafish during light adaptation.
615 J. Exp. Biol. 210, 2526–2539. https://doi.org/10.1242/jeb.003939
616 Burgess, H.A., Johnson, S.L., Granato, M., 2009. Unidirectional startle responses and disrupted left-right co-
617 ordination of motor behaviors in *robo3* mutant zebrafish. Genes Brain Behav. 8, 500–511.
618 https://doi.org/10.1111/j.1601-183X.2009.00499.x
619 Chen, X., Mu, Y., Hu, Y., Kuan, A.T., Nikitchenko, M., Randlett, O., Chen, A.B., Gavornik, J.P., Sompolinsky,
620 H., Engert, F., Ahrens, M.B., 2018. Brain-wide Organization of Neuronal Activity and Convergent
621 Sensorimotor Transformations in Larval Zebrafish. Neuron 100, 876-890.e5.
622 https://doi.org/10.1016/j.neuron.2018.09.042
623 Czopka, T., Lyons, D.A., 2011. Dissecting Mechanisms of Myelinated Axon Formation Using Zebrafish, in:
624 Methods in Cell Biology. Elsevier, pp. 25–62. https://doi.org/10.1016/B978-0-12-381320-6.00002-3
625 Diana, G., Sainsbury, T.T.J., Meyer, M.P., 2018. Bayesian inference of neuronal ensembles. Biorxiv.
626 https://doi.org/10.1101/452557
627 Dreosti, E., Lopes, G., Kampff, A.R., Wilson, S.W., 2015. Development of social behavior in young zebrafish.
628 Front. Neural Circuits 9. https://doi.org/10.3389/fncir.2015.00039
629 Dunn, T.W., Gebhardt, C., Naumann, E.A., Riegler, C., Ahrens, M.B., Engert, F., Del Bene, F., 2016. Neural
630 Circuits Underlying Visually Evoked Escapes in Larval Zebrafish. Neuron 89, 613–628.
631 https://doi.org/10.1016/j.neuron.2015.12.021
632 Early, J.J., Cole, K.L., Williamson, J.M., Swire, M., Kamadurai, H., Muskavitch, M., Lyons, D.A., 2018. An
633 automated high-resolution in vivo screen in zebrafish to identify chemical regulators of myelination.
634 eLife 7, e35136. https://doi.org/10.7554/eLife.35136
635 Emery, B., Agalliu, D., Cahoy, J.D., Watkins, T.A., Dugas, J.C., Mulinyawe, S.B., Ibrahim, A., Ligon, K.L.,
636 Rowitch, D.H., Barres, B.A., 2009. Myelin Gene Regulatory Factor Is a Critical Transcriptional
637 Regulator Required for CNS Myelination. Cell 138, 172–185.
638 https://doi.org/10.1016/j.cell.2009.04.031
639 Fields, R.D., 2015. A new mechanism of nervous system plasticity: activity-dependent myelination. Nat. Rev.
640 Neurosci. 16, 756–767. https://doi.org/10.1038/nrn4023
641 Gahtan, E., O'Malley, D.M., 2003. Visually guided injection of identified reticulospinal neurons in zebrafish: A
642 survey of spinal arborization patterns. J. Comp. Neurol. 459, 186–200.
643 https://doi.org/10.1002/cne.10621

644 Geraghty, A.C., Gibson, E.M., Ghanem, R.A., Greene, J.J., Ocampo, A., Goldstein, A.K., Ni, L., Yang, T.,
645 Marton, R.M., Paşca, S.P., Greenberg, M.E., Longo, F.M., Monje, M., 2019. Loss of Adaptive
646 Myelination Contributes to Methotrexate Chemotherapy-Related Cognitive Impairment. Neuron 103,
647 250-265.e8. https://doi.org/10.1016/j.neuron.2019.04.032
648 Gibson, E.M., Geraghty, A.C., Monje, M., 2018. Bad wrap: Myelin and myelin plasticity in health and disease:
649 Myelin and Myelin Plasticity in Health and Disease. Dev. Neurobiol. 78, 123–135.
650 https://doi.org/10.1002/dneu.22541
651 Hale, M.E., Katz, H.R., Peek, M.Y., Fremont, R.T., 2016. Neural circuits that drive startle behavior, with a
652 focus on the Mauthner cells and spiral fiber neurons of fishes. J. Neurogenet. 30, 89–100.
653 https://doi.org/10.1080/01677063.2016.1182526
654 Hamanaka, K., Takata, A., Uchiyama, Y., Miyatake, S., Miyake, N., Mitsuhashi, S., Iwama, K., Fujita, A.,
655 Imagawa, E., Alkanaq, A.N., Koshimizu, E., Azuma, Y., Nakashima, M., Mizuguchi, T., Saitsu, H.,
656 Wada, Y., Minami, S., Katoh-Fukui, Y., Masunaga, Y., Fukami, M., Hasegawa, T., Ogata, T.,
657 Matsumoto, N., 2019. MYRF haploinsufficiency causes 46,XY and 46,XX disorders of sex
658 development: bioinformatics consideration. Hum. Mol. Genet. 28, 2319–2329.
659 https://doi.org/10.1093/hmg/ddz066
660 Henriques, P.M., Rahman, N., Jackson, S.E., Bianco, I.H., 2019. Nucleus Isthmi Is Required to Sustain Target
661 Pursuit during Visually Guided Prey-Catching. Curr. Biol. 29, 1771-1786.e5.
662 https://doi.org/10.1016/j.cub.2019.04.064
663 Hildebrand, D.G.C., Cicconet, M., Torres, R.M., Choi, W., Quan, T.M., Moon, J., Wetzel, A.W., Scott
664 Champion, A., Graham, B.J., Randlett, O., Plummer, G.S., Portugues, R., Bianco, I.H., Saalfeld, S.,
665 Baden, A.D., Lillaney, K., Burns, R., Vogelstein, J.T., Schier, A.F., Lee, W.-C.A., Jeong, W.-K.,
666 Lichtman, J.W., Engert, F., 2017. Whole-brain serial-section electron microscopy in larval zebrafish.
667 Nature 545, 345–349. https://doi.org/10.1038/nature22356
668 Hines, J.H., Ravanelli, A.M., Schwindt, R., Scott, E.K., Appel, B., 2015. Neuronal activity biases axon selection
669 for myelination in vivo. Nat. Neurosci. 18, 683–689. https://doi.org/10.1038/nn.3992
670 Jain, R.A., Wolman, M.A., Marsden, K.C., Nelson, J.C., Shoenhard, H., Echeverry, F.A., Szi, C., Bell, H.,
671 Skinner, J., Cobbs, E.N., Sawada, K., Zamora, A.D., Pereda, A.E., Granato, M., 2018. A Forward
672 Genetic Screen in Zebrafish Identifies the G-Protein-Coupled Receptor CaSR as a Modulator of

673 Sensorimotor Decision Making. Curr. Biol. 28, 1357-1369.e5.
674 https://doi.org/10.1016/j.cub.2018.03.025
675 Jao, L.-E., Wente, S.R., Chen, W., 2013. Efficient multiplex biallelic zebrafish genome editing using a CRISPR
676 nuclease system. Proc. Natl. Acad. Sci. 110, 13904–13909. https://doi.org/10.1073/pnas.1308335110
677 Karttunen, M.J., Czopka, T., Goedhart, M., Early, J.J., Lyons, D.A., 2017. Regeneration of myelin sheaths of
678 normal length and thickness in the zebrafish CNS correlates with growth of axons in caliber. PLOS
679 ONE 12, e0178058. https://doi.org/10.1371/journal.pone.0178058
680 Kim, J.H., Renden, R., von Gersdorff, H., 2013. Dysmyelination of Auditory Afferent Axons Increases the Jitter
681 of Action Potential Timing during High-Frequency Firing. J. Neurosci. 33, 9402–9407.
682 https://doi.org/10.1523/JNEUROSCI.3389-12.2013
683 Kimmel, C.B., Patterson, J., Kimmel, R.O., 1974. The development and behavioral characteristics of the startle
684 response in the zebra fish. Dev. Psychobiol. 7, 47–60. https://doi.org/10.1002/dev.420070109
685 Klingseisen, A., Ristoiu, A.-M., Kegel, L., Sherman, D.L., Rubio-Brotons, M., Almeida, R.G., Koudelka, S.,
686 Benito-Kwiecinski, S.K., Poole, R.J., Brophy, P.J., Lyons, D.A., 2019. Oligodendrocyte Neurofascin
687 Independently Regulates Both Myelin Targeting and Sheath Growth in the CNS. Dev. Cell 51, 730-
688 744.e6. https://doi.org/10.1016/j.devcel.2019.10.016
689 Koenning, M., Jackson, S., Hay, C.M., Faux, C., Kilpatrick, T.J., Willingham, M., Emery, B., 2012. Myelin
690 Gene Regulatory Factor Is Required for Maintenance of Myelin and Mature Oligodendrocyte Identity
691 in the Adult CNS. J. Neurosci. 32, 12528–12542. https://doi.org/10.1523/JNEUROSCI.1069-12.2012
692 Koudelka, S., Voas, M.G., Almeida, R.G., Baraban, M., Soetaert, J., Meyer, M.P., Talbot, W.S., Lyons, D.A.,
693 2016. Individual Neuronal Subtypes Exhibit Diversity in CNS Myelination Mediated by Synaptic
694 Vesicle Release. Curr. Biol. 26, 1447–1455. https://doi.org/10.1016/j.cub.2016.03.070
695 Lacoste, A.M.B., Schoppik, D., Robson, D.N., Haesemeyer, M., Portugues, R., Li, J.M., Randlett, O., Wee,
696 C.L., Engert, F., Schier, A.F., 2015. A Convergent and Essential Interneuron Pathway for Mauthner-
697 Cell-Mediated Escapes. Curr. Biol. 25, 1526–1534. https://doi.org/10.1016/j.cub.2015.04.025
698 Larsch, J., Baier, H., 2018. Biological Motion as an Innate Perceptual Mechanism Driving Social Affiliation.
699 Curr. Biol. 28, 3523-3532.e4. https://doi.org/10.1016/j.cub.2018.09.014
700 Liu, J., Dupree, J.L., Gacias, M., Frawley, R., Sikder, T., Naik, P., Casaccia, P., 2016. Clemastine Enhances
701 Myelination in the Prefrontal Cortex and Rescues Behavioral Changes in Socially Isolated Mice. J.
702 Neurosci. 36, 957–962. https://doi.org/10.1523/JNEUROSCI.3608-15.2016

703 Makinodan, M., Rosen, K.M., Ito, S., Corfas, G., 2012. A Critical Period for Social Experience-Dependent
704 Oligodendrocyte Maturation and Myelination. Science 337, 1357–1360.
705 https://doi.org/10.1126/science.1220845
706 Marquart, G.D., Tabor, K.M., Bergeron, S.A., Briggman, K.L., Burgess, H.A., 2019. Prepontine non-giant
707 neurons drive flexible escape behavior in zebrafish (preprint). Neuroscience.
708 https://doi.org/10.1101/668517
709 Marques, J.C., Lackner, S., Félix, R., Orger, M.B., 2018. Structure of the Zebrafish Locomotor Repertoire
710 Revealed with Unsupervised Behavioral Clustering. Curr. Biol. 28, 181-195.e5.
711 https://doi.org/10.1016/j.cub.2017.12.002
712 McKenzie, I.A., Ohayon, D., Li, H., Paes de Faria, J., Emery, B., Tohyama, K., Richardson, W.D., 2014. Motor
713 skill learning requires active central myelination. Science 346, 318–322.
714 https://doi.org/10.1126/science.1254960
715 Mensch, S., Baraban, M., Almeida, R., Czopka, T., Ausborn, J., El Manira, A., Lyons, D.A., 2015. Synaptic
716 vesicle release regulates myelin sheath number of individual oligodendrocytes in vivo. Nat. Neurosci.
717 18, 628–630. https://doi.org/10.1038/nn.3991
718 Metcalfe, W.K., Mendelson, B., Kimmel, C.B., 1986. Segmental homologies among reticulospinal neurons in
719 the hindbrain of the zebrafish larva. J. Comp. Neurol. 251, 147–159.
720 https://doi.org/10.1002/cne.902510202
721 Mount, C.W., Monje, M., 2017. Wrapped to Adapt: Experience-Dependent Myelination. Neuron 95, 743–756.
722 https://doi.org/10.1016/j.neuron.2017.07.009
723 Naumann, E.A., Fitzgerald, J.E., Dunn, T.W., Rihel, J., Sompolinsky, H., Engert, F., 2016. From Whole-Brain
724 Data to Functional Circuit Models: The Zebrafish Optomotor Response. Cell 167, 947-960.e20.
725 https://doi.org/10.1016/j.cell.2016.10.019
726 Nave, K.-A., Werner, H.B., 2014. Myelination of the Nervous System: Mechanisms and Functions. Annu. Rev.
727 Cell Dev. Biol. 30, 503–533. https://doi.org/10.1146/annurev-cellbio-100913-013101
728 Pan, S., Mayoral, S.R., Choi, H.S., Chan, J.R., Kheirbek, M.A., 2020. Preservation of a remote fear memory
729 requires new myelin formation. Nat. Neurosci. 23, 487–499. https://doi.org/10.1038/s41593-019-0582-
730 1
731 Pinz, H., Pyle, L.C., Li, D., Izumi, K., Skraban, C., Tarpinian, J., Braddock, S.R., Telegrafi, A., Monaghan,
732 K.G., Zackai, E., Bhoj, E.J., 2018. De novo variants in Myelin regulatory factor (MYRF) as candidates

of a new syndrome of cardiac and urogenital anomalies. Am. J. Med. Genet. A. 176, 969–972. https://doi.org/10.1002/ajmg.a.38620

Preston, M.A., Macklin, W.B., 2015. Zebrafish as a model to investigate CNS myelination: Zebrafish Myelination. Glia 63, 177–193. https://doi.org/10.1002/glia.22755

Redmond, S.A., Mei, F., Eshed-Eisenbach, Y., Osso, L.A., Leshkowitz, D., Shen, Y.-A.A., Kay, J.N., Aurrand-Lions, M., Lyons, D.A., Peles, E., Chan, J.R., 2016. Somatodendritic Expression of JAM2 Inhibits Oligodendrocyte Myelination. Neuron 91, 824–836. https://doi.org/10.1016/j.neuron.2016.07.021

Romano, S.A., Pietri, T., Pérez-Schuster, V., Jouary, A., Haudrechy, M., Sumbre, G., 2015. Spontaneous Neuronal Network Dynamics Reveal Circuit's Functional Adaptations for Behavior. Neuron 85, 1070–1085. https://doi.org/10.1016/j.neuron.2015.01.027

Rossetti, L.Z., Glinton, K., Yuan, B., Liu, P., Pillai, N., Mizerik, E., Magoulas, P., Rosenfeld, J.A., Karaviti, L., Sutton, V.R., Lalani, S.R., Scott, D.A., 2019. Review of the phenotypic spectrum associated with haploinsufficiency of *MYRF*. Am. J. Med. Genet. A. ajmg.a.61182. https://doi.org/10.1002/ajmg.a.61182

Rossi, A., Kontarakis, Z., Gerri, C., Nolte, H., Hölper, S., Krüger, M., Stainier, D.Y.R., 2015. Genetic compensation induced by deleterious mutations but not gene knockdowns. Nature 524, 230–233. https://doi.org/10.1038/nature14580

Roy, B., Ali, D.W., 2013. Patch Clamp Recordings from Embryonic Zebrafish Mauthner Cells. J. Vis. Exp. 50551. https://doi.org/10.3791/50551

Saint-Amant, L., Drapeau, P., 2003. Whole-cell patch-clamp recordings from identified spinal neurons in the zebrafish embryo. Methods Cell Sci. 25, 59–64. https://doi.org/10.1023/B:MICS.0000006896.02938.49

Sampaio-Baptista, C., Khrapitchev, A.A., Foxley, S., Schlagheck, T., Scholz, J., Jbabdi, S., DeLuca, G.C., Miller, K.L., Taylor, A., Thomas, N., Kleim, J., Sibson, N.R., Bannerman, D., Johansen-Berg, H., 2013. Motor Skill Learning Induces Changes in White Matter Microstructure and Myelination. J. Neurosci. 33, 19499–19503. https://doi.org/10.1523/JNEUROSCI.3048-13.2013

Schindelin, J., Arganda-Carreras, I., Frise, E., Kaynig, V., Longair, M., Pietzsch, T., Preibisch, S., Rueden, C., Saalfeld, S., Schmid, B., Tinevez, J.-Y., White, D.J., Hartenstein, V., Eliceiri, K., Tomancak, P., Cardona, A., 2012. Fiji: an open-source platform for biological-image analysis. Nat. Methods 9, 676–682. https://doi.org/10.1038/nmeth.2019

762 Steadman, P.E., Xia, F., Ahmed, M., Mocle, A.J., Penning, A.R.A., Geraghty, A.C., Steenland, H.W., Monje,
763 M., Josselyn, S.A., Frankland, P.W., 2020. Disruption of Oligodendrogenesis Impairs Memory
764 Consolidation in Adult Mice. Neuron 105, 150-164.e6. https://doi.org/10.1016/j.neuron.2019.10.013
765 Sumbre, G., Muto, A., Baier, H., Poo, M., 2008. Entrained rhythmic activities of neuronal ensembles as
766 perceptual memory of time interval. Nature 456, 102–106. https://doi.org/10.1038/nature07351
767 Tabor, K.M., Smith, T.S., Brown, M., Bergeron, S.A., Briggman, K.L., Burgess, H.A., 2018. Presynaptic
768 Inhibition Selectively Gates Auditory Transmission to the Brainstem Startle Circuit. Curr. Biol. 28,
769 2527-2535.e8. https://doi.org/10.1016/j.cub.2018.06.020
770 Tanimoto, M., Ota, Y., Horikawa, K., Oda, Y., 2009. Auditory Input to CNS Is Acquired Coincidentally with
771 Development of Inner Ear after Formation of Functional Afferent Pathway in Zebrafish. J. Neurosci.
772 29, 2762–2767. https://doi.org/10.1523/JNEUROSCI.5530-08.2009
773 Treichel, A.J., Hines, J.H., 2018. Development of an Embryonic Zebrafish Oligodendrocyte–Neuron Mixed
774 Coculture System. Zebrafish 15, 586–596. https://doi.org/10.1089/zeb.2018.1625
775 Wang, F., Ren, S.-Y., Chen, J.-F., Liu, K., Li, R.-X., Li, Z.-F., Hu, B., Niu, J.-Q., Xiao, L., Chan, J.R., Mei, F.,
776 2020. Myelin degeneration and diminished myelin renewal contribute to age-related deficits in
777 memory. Nat. Neurosci. 23, 481–486. https://doi.org/10.1038/s41593-020-0588-8
778 Waxman, S.G., 1980. Determinants of conduction velocity in myelinated nerve fibers. Muscle Nerve 3, 141–
779 150. https://doi.org/10.1002/mus.880030207
780 Wen, H., 2005. Paired Motor Neuron-Muscle Recordings in Zebrafish Test the Receptor Blockade Model for
781 Shaping Synaptic Current. J. Neurosci. 25, 8104–8111. https://doi.org/10.1523/JNEUROSCI.2611-
782 05.2005
783 Wolf, S., Dubreuil, A.M., Bertoni, T., Böhm, U.L., Bormuth, V., Candelier, R., Karpenko, S., Hildebrand,
784 D.G.C., Bianco, I.H., Monasson, R., Debrégeas, G., 2017. Sensorimotor computation underlying
785 phototaxis in zebrafish. Nat. Commun. 8, 651. https://doi.org/10.1038/s41467-017-00310-3
786 Wolman, M.A., Jain, R.A., Liss, L., Granato, M., 2011. Chemical modulation of memory formation in larval
787 zebrafish. Proc. Natl. Acad. Sci. 108, 15468–15473. https://doi.org/10.1073/pnas.1107156108
788 Yamanaka, I., Miki, M., Asakawa, K., Kawakami, K., Oda, Y., Hirata, H., 2013. Glycinergic transmission and
789 postsynaptic activation of CaMKII are required for glycine receptor clustering *in vivo*. Genes Cells 18,
790 211–224. https://doi.org/10.1111/gtc.12032

791 Zottoli, S.J., Bentley, A.P., Prendergast, B.J., Rieff, H., I., 1995. Comparative Studies on the Mauthner Cell of
792 Teleost Fish in Relation to Sensory Input. Brain Behav. Evol. 46, 151–164.
793
794

Figure Legends

Figure 1: *myrf*^{ue70} mutants display a gross reduction in the level of CNS myelination at the adult and larval stages.

A, Top: myrf gene structure composed of 27 exons. Red arrowhead marks the location of the mutation in exon 2. Scale bar equates to 1000bp. Schematic created using http://*wormweb.org*. **Middle:** Wildtype and mutant nucleotide sequences spanning the mutagenesis site. The guide RNA (gRNA) target site (red line) and restriction enzyme (RE) recognition site (green line) are labelled. **Bottom:** Amino acid sequence indicating that the *myrf*^{ue70} mutation results in shift in the open reading frame leading to downstream coding for a premature stop codon (*).

B, The relative concentration of mbp mRNA is reduced by 95% in mutants (0.04 ± 0.03 au) compared to wildtypes (1.003 ± 0.13 au, p = 0.0002, unpaired t test, N = 3 adult brains per genotype).

C, Transverse section of the spinal cord in an adult *myrf*^{ue70} sibling showing extensive myelination of ventral spinal cord (dashed box). 20x objective. Scale bar = 100μm.

D, TEM images of the spinal cord in the region of the ventral spinal tract (outlined in C) in *myrf*^{ue70} adult siblings (top) and mutants (bottom). Panels i-iv display different fields of view within the region of interest. Thick myelin sheaths are clearly visible in siblings, particularly surrounding the Mauthner axon. There is a lack of myelin surrounding the Mauthner axon in the mutant sample, and distinct reduction in the level of myelination in the remainder of surrounding spinal cord. Occasional hypomyelinated and dysmyelinated axons can be observed in the mutant samples. Scale bar = 5 microns for panels i-iii. Scale bar = 1 micron for panel iv. 'm' denotes the Mauthner axon.

E, Top: Brightfield images of *myrf*^{ue70} wildtype and mutant larvae at 6 dpf. Black box defines the anatomical region imaged across animals. Scale bar = 0.5mm. **Bottom:** Confocal microscopy images of the spinal cord at 6 dpf in *myrf*^{ue70} Tg(mbp:eGFP-CAAX) larvae. Scale bar = 20μm.

Figure 2: *myrf*^{ue70} mutants display CNS-specific hypomyelination at 6 dpf.

A, TEM images of the myelinated tracts in the dorsal (top row) and ventral spinal cord (bottom rows). Scale bars = 1μm.

B, Schematic of the transverse section of a 6 dpf larval zebrafish at the level of the urogenital opening. **Inset**: transverse section of the spinal cord at the same level. Myelinated (green) axons are located in the ventral and dorsal spinal tracts of the spinal cord (CNS) as well as the posterior lateral line (PNS). m = Mauthner axons.

C, TEM images of the posterior lateral line at 6 dpf. Scale bar = 1μm.

D, The average number of myelinated axons in one hemi-spinal cord is reduced by 66% in mutants (wildtypes: 35.29 ± 7.83 myelinated axons, mutants: 12.00 ± 4.34 myelinated axons, $p \leq 0.0001$, unpaired t-test, N = 7 wildtypes, N = 8 mutants)**.**

E, The number of myelinated axons in the PNS is similar between genotypes (wildtypes: 7.33 ± 1.53 myelinated axons, mutants: 9.00 ± 3.83 myelinated axons, $p = 0.52$, unpaired t-test, N = 3 wildtypes, N = 4 mutants). Values represent mean ± standard deviation**.**

F, G-ratio of Mauthner axons in wildtype and mutant siblings (wildtypes: 0.48 ± 0.009, mutants: 0.80 ± 0.08, $p = 0.0009$, unpaired t-test).

G, G-ratios for myelinated axons for small caliber (area <0.3μm^2) and large caliber (area >0.3μm^2) myelinated axons. The g-ratio of small caliber axons is similar between groups (wildtypes: 0.57 (0.52 to 0.62), mutants: 0.59 (0.52 to 0.70), $p = 0.51$, Mann Whitney test, n = 53 myelinated axons in wildtypes, n = 17 myelinated axons in mutants). The g-ratios for large caliber axons are significantly higher in mutants than wildtype siblings (wildtypes: 0.60 ± 0.08, mutants: 0.71 ± 0.08, $p \leq 0.0001$, unpaired t-test, n = 33 myelinated axons in wildtypes, n = 19 myelinated axons in mutants).

Figure 3: *myrf*^{ue70} mutants have fewer oligodendrocytes which produce less myelin and fail to maintain myelin sheaths over time.

A, Confocal images of the spinal cord at 6 dpf in sibling control and *myrf*^{ue70} Tg(mbp:nls-eGFP) larvae. Scale bar = 100µm.

B, Oligodendrocyte numbers in the spinal cord at 6 dpf (wildtype: 304.8 ± 39.07, mutants: 239.3 ± 50.48, p = 0.0002, unpaired t test, N = 15 wildtypes, N = 22 mutants). Error bars represent mean ± standard deviation.

C, Representative confocal images of single oligodendrocytes mosaically labelled with mbp:mCherry-CAAX reporter construct in a wildtype (top) and mutant (bottom) at 6 dpf. Scale bar = 15µm.

D, Average myelin sheath number was reduced in *myrf*^{ue70} mutants relative to wildtype siblings at 6 dpf (wildtypes: 10.50 (7.00 to 14.00) sheaths per cell, mutants: 7.00 (5.00 to 10.50) sheaths per cell, p = 0.02, Mann Whitney test). Values and error bars represent median and IQR.

E, Average myelin sheath length was reduced from 41.83 ± 9.68µm in wildtypes to 31.35 ± 11.49µm in mutants at 6 dpf (p = 0.002, unpaired t test). Error bars represent mean ± standard deviation.

F, Total myelin produced per oligodendrocyte was reduced from 458.2 ± 156.4µm in wildtypes to 241.1 ± 138.6µm in mutants at 6 dpf ($p \leq 0.0001$, unpaired t test). Error bars represent mean ± standard deviation.

D-F: N = 20 wildtypes, N = 27 mutants.

G, Confocal images of a single mutant oligodendrocyte labelled with mbp:mCherry-CAAX at 4 and 6 dpf. A myelin sheath (*) and myelinated neuronal cell body (#) are observed at 4 dpf and subsequently retracted by 6 dpf. Arrowheads label myelin sheaths which are observed to shrink between 4 and 6 dpf. Scale bar = 15µm.

H, Myelin sheaths belonging to wildtype oligodendrocytes demonstrated a net growth of 6.24 ± 3.43µm between 4 and 6 dpf, while mutants display net shrinkage of myelin sheaths by -0.31 ± 4.79µm (p = 0.003, unpaired t test). Error bars represent mean ± standard deviation**.**

I, Between 4 and 6 dpf, wildtype oligodendrocytes retracted 0 (0 to 0) myelin sheaths, while mutants retracted 2 (1 to 3) myelin sheaths (p = 0.009, Mann Whitney test). Error bars represent median and IQR.

J, Number of abnormal myelin sheaths at 6 dpf (wildtypes: 0.00 (0.00-0.00); mutants: 2 (0.00-3.00), $p \leq 0.0001$, Mann Whitney test). Error bars represent median and IQR.

H – I: N = 11 wildtypes, N = 7 mutants. **J:** N = 20 wildtypes, N = 27 mutants.

Figure 4: *myrf*^{ue70} mutants exhibit increased latency to perform startle responses, and a tendency to perform avoidance behaviour, in response to defined acoustic stimuli.

A, Overview of the neuronal circuitry involved in motor response to auditory stimuli. **Startle response (SLC):** sensory input from the ear, via the auditory nerve (red), is received at the lateral dendrite of the Mauthner cell body (black). The axon of the Mauthner cell crosses into the contralateral aspect of the spinal cord where it extends along the ventral tract to recruit motor neurons directly along the length of the larvae. Recruitment of motor neurons allows muscle contraction on the side of the body contralateral to the stimulus, allowing a rapid, high-velocity c-bend (motor response) away from the stimulus (inset). **Avoidance behaviour (LLC)**: sensory input is detected by prepontine neurons (purple) in the hindbrain, which recruit ipsilateral motor neurons indirectly, resulting in a low-velocity, longer latency, c-bend away from the stimulus.

B, Schematic of the behavioural rig.

C, Relative frequency histogram displaying the distribution of latencies for behavioural responses in response to acoustic stimuli in wildtype and mutant larvae (N = 24 wildtype larvae, n = 220 events; N = 35 mutant larvae, n = 299 events; Kolmogorov-Smirnov test, $p \leq 0.0001$).

D, Number and proportion of events (SLC vs LLC) per genotype.

E, React rate per fish (median react rate = 100% in both wildtypes and mutants, p = 0.24, Mann-Whitney test, N = 25 wildtype larvae, N = 38 mutant larvae). Larvae are excluded from subsequent analysis if they exhibit a react rate <70%.

F, Average latency values per fish (wildtype: 10.55ms (9.6-16.15ms), mutants: 17.6ms (12.9-21.88ms), p = 0.003, Mann-Whitney test).

G, Average latency of short latency c-starts (<16ms) (wildtypes: 10.03 ± 0.85ms, mutants: 10.67 ± 0.83ms, p = 0.006, unpaired t test).

H, Average latency of long latency c-starts (>16ms) (wildtypes: 43.20 ± 8.95ms; mutants: 38.91 ± 10.15ms, p = 0.28, unpaired t test).

I, Mean and standard deviations values for SLC and LLC responses per genotype.

J-M analysis of c-bend kinematics:

J, Example trace of orientation over time during a behavioural response to an acoustic stimulus. C-bend kinematics are calculated from individual traces for each response per fish. Latency is the time from stimulus onset to behavioural onset (red star). C-bend duration (A) is time from behaviour onset to initial turn angle (blue

903 star). Maximum angular velocity is defined as the change in orientation over time (B/A). Turning angle equates
904 to the initial turn angle.
905 **K,** Initial turn duration (SLC: wildtypes: 10.06 ± 0.70ms, mutants: 9.81 ± 0.72ms, p = 0.20, unpaired t-test;
906 LLC: wildtypes: 14.30 ± 3.65ms, mutants: 13.25 ± 3.10, p = 0.42, unpaired t test).
907 **L,** Maximum angular velocity (SLC: wildtypes: 24°/ms (22.78-28.68°/ms), mutants: 25°/ms (23.10-26.60°/ms),
908 p = 0.73, Mann-Whitney test; LLC: wildtypes: 16.16 ± 6.61°/ms, mutants: 13.67 ± 4.95°/ms, p = 0.24, unpaired
909 t test).
910 **M,** Initial turn angle (SLC: wildtypes: 121.9 ± 10.80°, mutants: 127.4 ± 9.86°, p = 0.051, unpaired t test; LLC:
911 wildtypes: 85.11 ± 35.78°, mutants: 83.78 ± 29.07°, p = 0.91, unpaired t test).
912 **N,** Descriptive statistics (mean ± standard deviation) for c-bend kinematics.
913 For **Figures E-G and K-M,** N = 23 wildtypes, N = 35 mutant larvae. For **Figures D & E** values represent
914 median and interquartile range, for **Figures F-K,** values represent mean ± standard deviation.
915
916

Figure 5: Whole cell current-clamp recordings from Mauthner cells demonstrate slower conduction velocity times and abnormal spiking profiles in *myrf*^{ue70} mutants.

A, Electrophysiological preparation for recording from Mauthner neuron in a whole-cell current clamp configuration while stimulating with an extracellular monopolar field electrode midway through the spinal cord.

B, Resting membrane potential is unchanged in (siblings (n = 18 cells): -70.82 ± 2.76mV, mutants (n = 6 cells): -70.68 ± 1.25mV, p = 0.9077 at 6 dpf).

C, Sample trace of an action potential recorded at 6 dpf in a wildtype fish illustrating the measurement of half-width. Half-width is described as width of action potential (ms) at its half height.

D, Half-width of action potential is unchanged (siblings (n = 18 cells): 0.64 ± 0.09ms, mutants (n = 9 cells): 0.60 ± 0.06ms, p = 0.2610 at 6 dpf).

E, An example of current – clamp recording from Mauthner neuron in a 6 dpf wildtype and mutant following field stimulation (stimulus artefact is indicated by a grey dashed line). Latency is described as time from the onset of stimulus artefact to the peak of action potential.

F, Normalised action potential latency is increased in mutants at 6 dpf (siblings (n = 19 cells): 0.80 ± 0.11ms/mm, mutants (n= 9 cells): 0.97 ± 0.07ms/mm, p = 0.0003 at 6 dpf).

G, Conduction velocity of Mauthner action potentials is significantly decreased in mutant larvae (siblings (n = 19 cells): 1.27 ± 0.17m/s, mutants (n = 9 cells): 1.04 ± 0.08m/s, p 0.0005 at 6 dpf).

H, Sample traces of three subsequent action potentials recorded from the same wildtype Mauthner cell at 6 dpf superimposed and aligned to the peak of stimulus artefact. The area outlined by the rectangle is magnified in the inset and demonstrates slight imprecision of action potential arrival.

I, Precision of action potential arrival is comparable in siblings and mutants (siblings (n = 16 cells): 0.0064 ± 0.0019ms, mutants (n = 8 cells): 0.0062 ± 0.0009ms, p = 0.8166 at 6 dpf).

J, Sample trace of a train of action potentials fired following 10 stimuli at 1000 Hz at 6 dpf in a myrf^{ue70} mutant and sibling.

K, Mauthner neurons in mutant larvae do not sustain prolonged action potential trains of high frequency stimulation (siblings (n = 19 cells): 55.79 ± 10.17% mutants (n = 9 cells): 38.89 ± 17.64% at 6 dpf, p = 0.0014 at 6 dpf).

For **Figures 5 B, D, F, G, I, K** error bars represent mean ± standard deviation. Unpaired t-test for **Figures 5 B, D, F, G, I** and a two-way ANOVA for **5K**. Scale bars are 10mV and 1ms for **Figures 5C, E, H, J** and 5 mV and 200μs for **Figure 5H inset**.

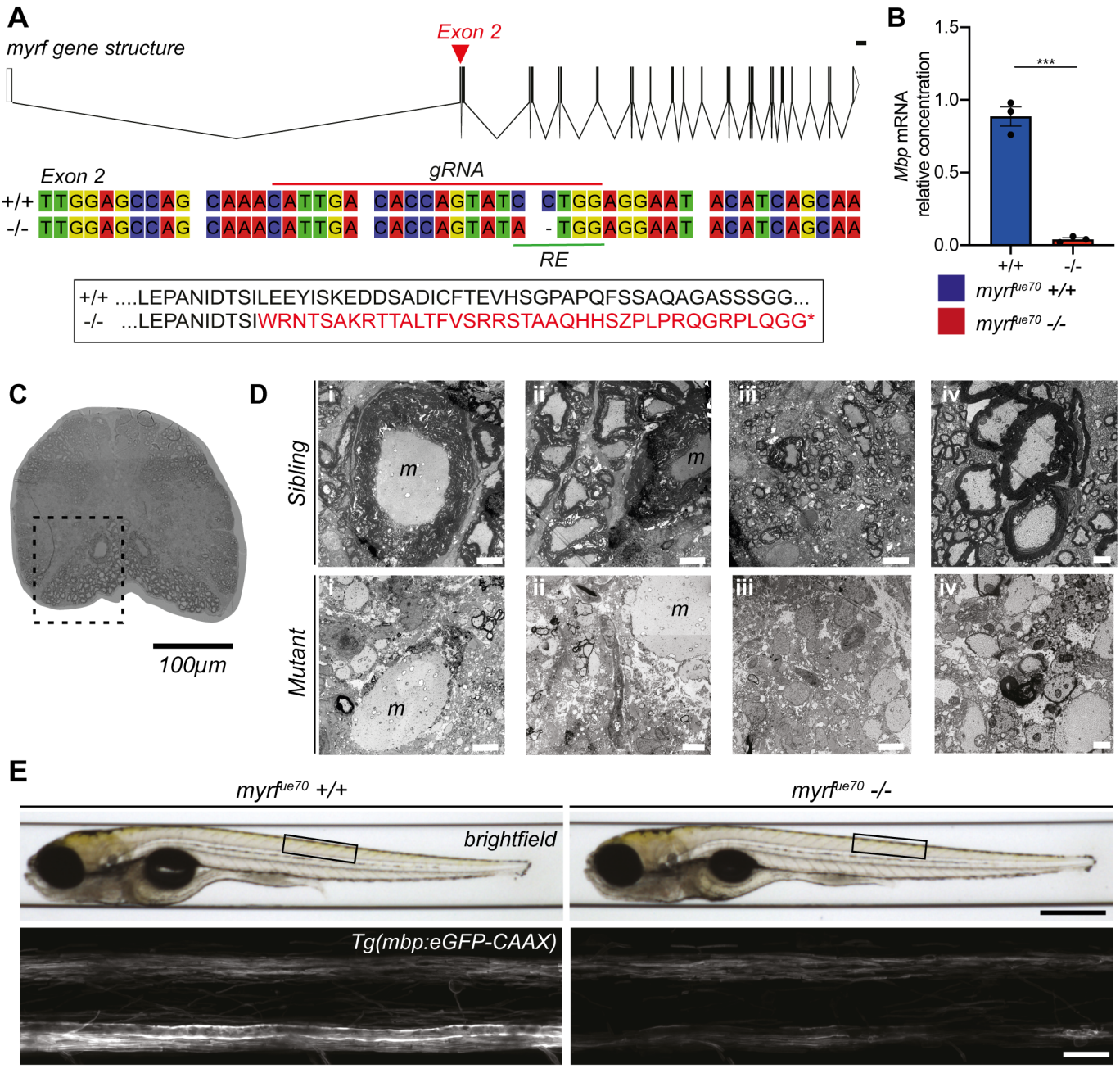

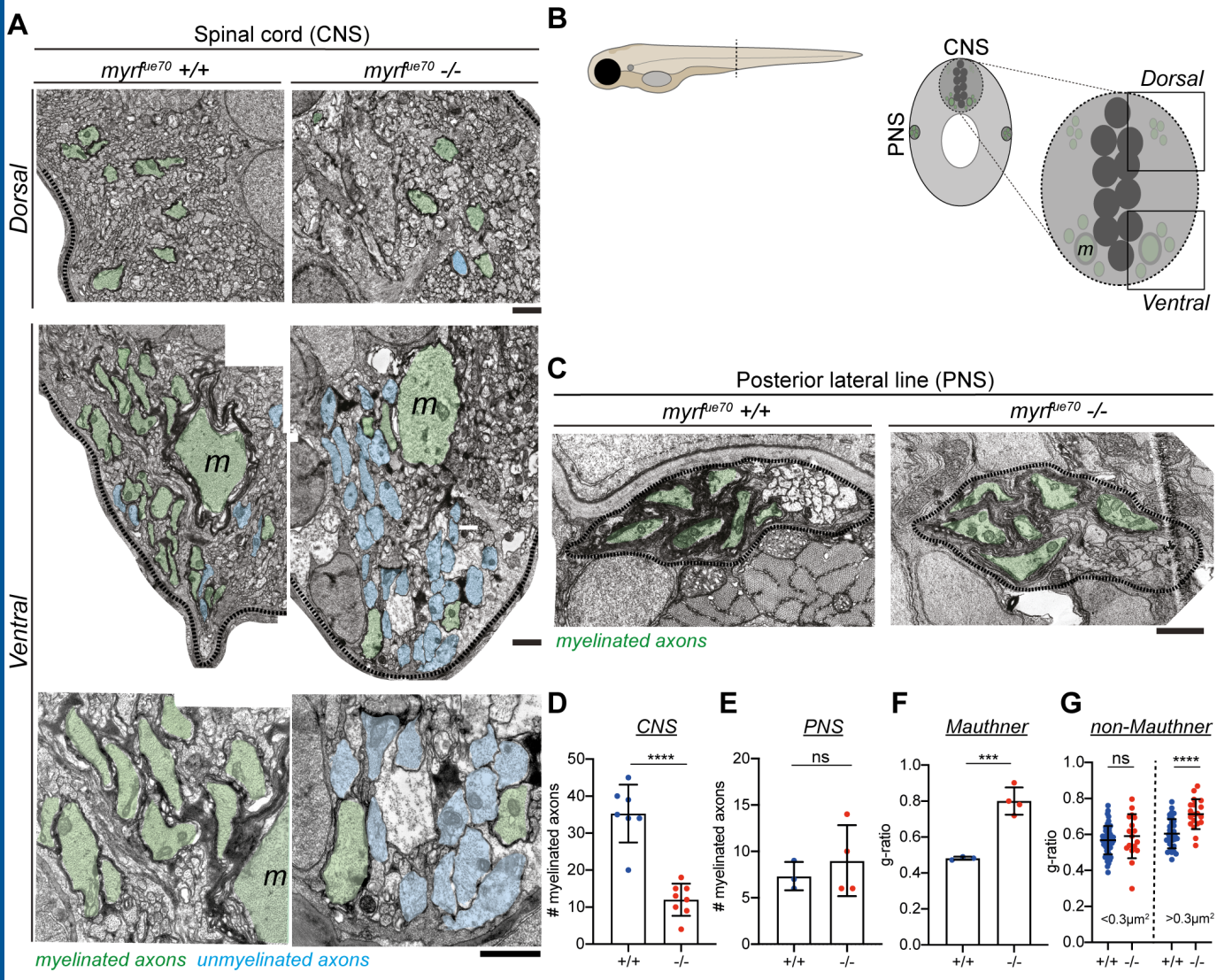

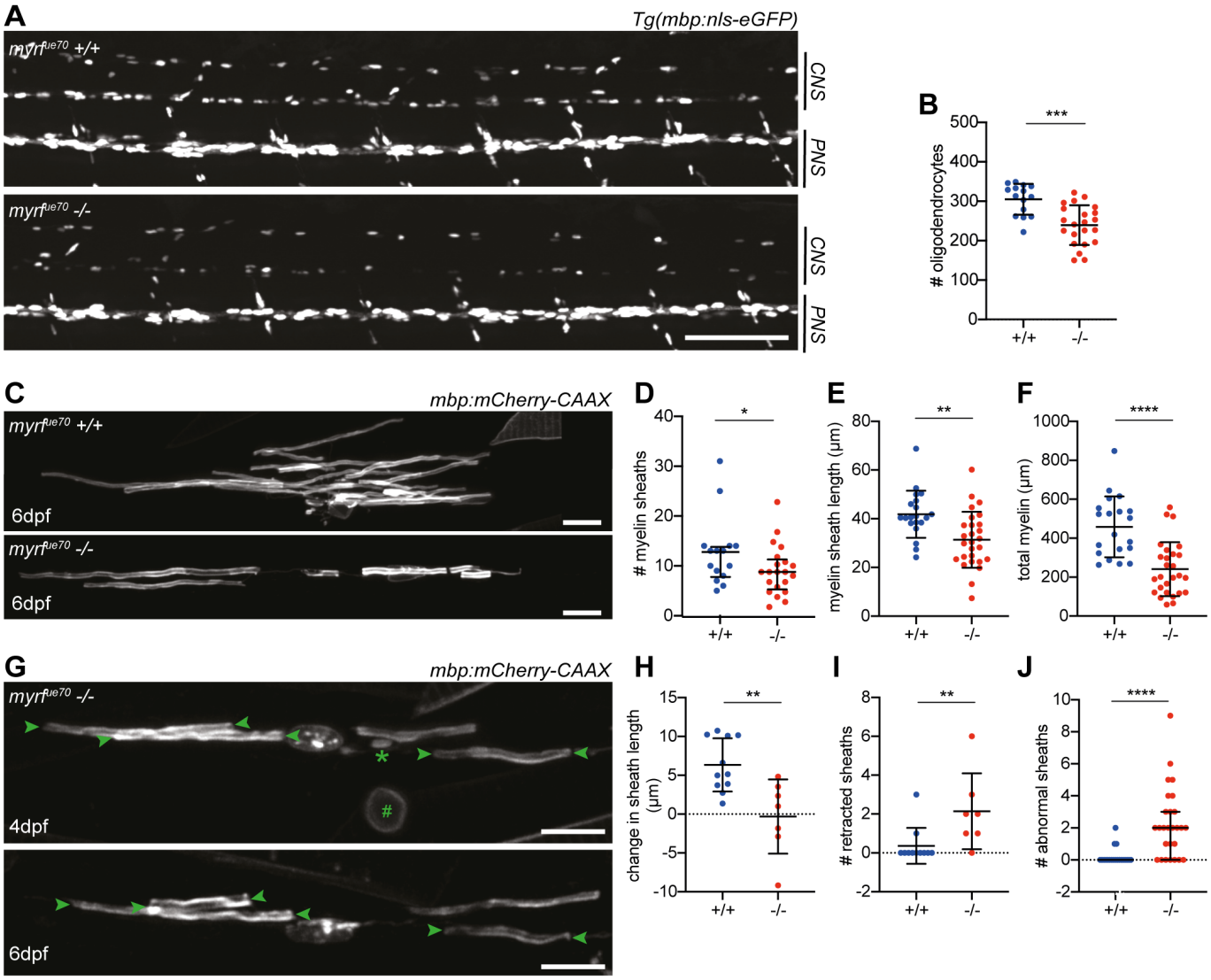

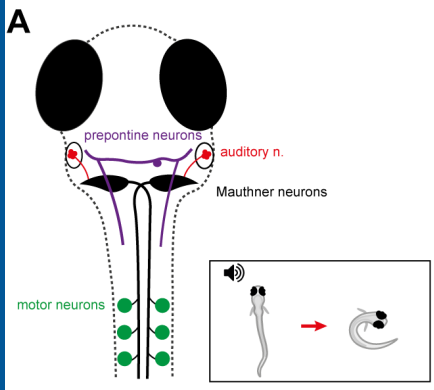

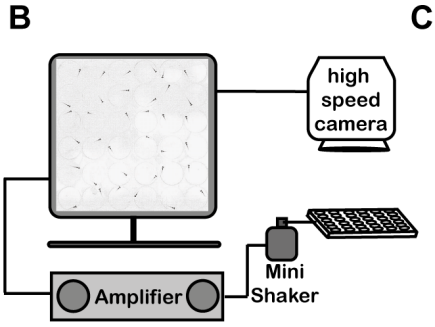

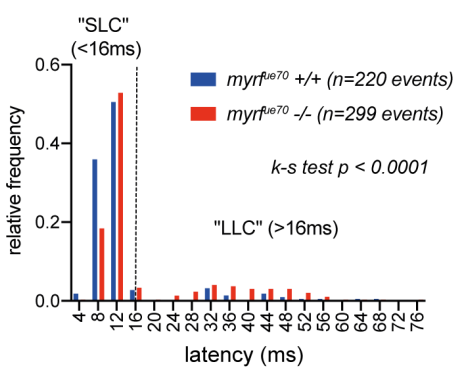

D

	myrf^{ue70}+/+	*myrf*^{ue70}-/-
SLC (<16ms)	n = 24 larvae, 200 events (90%)	n = 35 larvae, 224 events (75%)
LLC (>16ms)	n = 8 larvae, 20 events (10%)	n = 34 larvae, 75 events (25%)

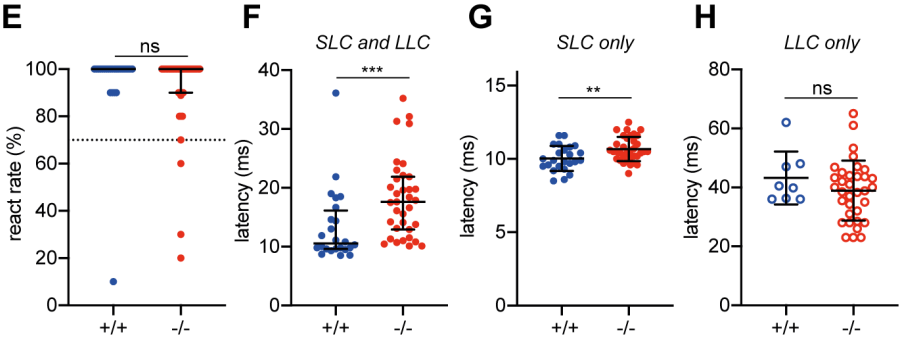

I

	Latency (ms)	
	myrf^{ue70}+/+	*myrf*^{ue70}-/-
SLC (<16ms)	10.03 +/- 0.85	10.67 +/- 0.83
LLC (>16ms)	43.2 +/- 8.95	38.9 +/- 10.15

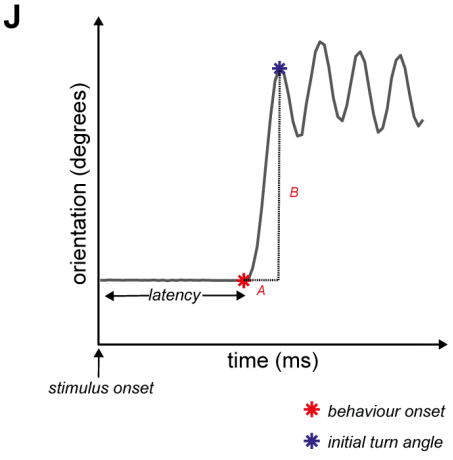

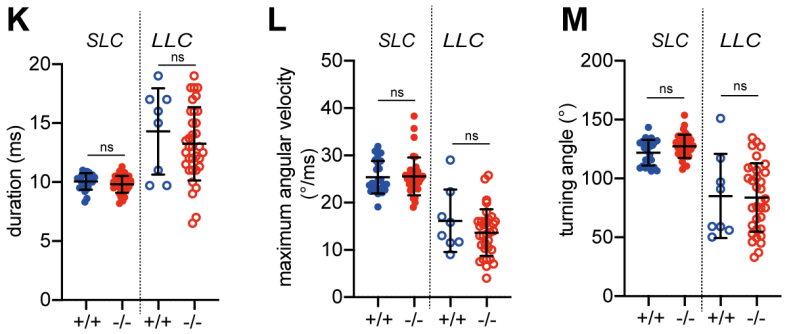

N

	Duration (ms)		Max angular velocity (°/ms)	
	myrf^{ue70}+/+	*myrf*^{ue70}-/-	*myrf*^{ue70}+/+	*myrf*^{ue70}-/-
SLC (<16ms)	10.06 +/- 0.70	9.81 +/- 0.72	25.39 +/- 3.43	25.58 +/- 4.00
LLC (>16ms)	14.3 +/- 3.65	13.25 +/- 3.10	16.16 +/- 6.61	13.67 +/- 4.95

	Initial turn angle (°)	
	myrf^{ue70}+/+	*myrf*^{ue70}-/-
SLC (<16ms)	121.9 +/- 10.80	127.4 +/- 9.86
LLC (>16ms)	85.11 +/- 35.78	83.78 +/- 29.07